Particuology 48 (2020) 109–115

Contents lists available at ScienceDirect

Particuology

journal homepage: www.elsevier.com/locate/partic

Analysis of the energy-minimization multiscale model with multiobjective optimization

Yi Mo [a], Mengjie Du [b,c], Wei Ge [b,c,*], Pingwen Zhang [a,**]

[a] School of Mathematical Sciences, Peking University, Beijing 100871, China
[b] State Key Laboratory of Multi-phase Complex Systems (MPCS), Institute of Processing Engineering (IPE), Chinese Academy of Sciences (CAS), Beijing 100190, China
[c] School of Chemical Engineering, University of the Chinese Academy of Sciences (UCAS), Beijing 100049, China

ARTICLE INFO

Article history:
Received 11 July 2018
Received in revised form 5 September 2018
Accepted 28 September 2018
Available online 26 February 2019

Keywords:
Energy-minimization multi-scale model
Multiobjective optimization
Flow regime transition

ABSTRACT

Gas–solid two-phase flow is ubiquitous in nature and many engineering fields, such as chemical engineering, energy, and mining. The closure of its hydrodynamic model is difficult owing to the complex multiscale structure of such flow. To address this problem, the energy-minimization multi-scale (EMMS) model introduces a stability condition that presents a compromise of the different dominant mechanisms involved in the systems, each expressed as an extremum tendency. However, in the physical system, each dominant mechanism should be expressed to a certain extent, and this has been formulated as a multiobjective optimization problem according to the EMMS principle generalized from the EMMS model. The mathematical properties and physical meanings of this multiobjective optimization problem have not yet been explored. This paper presents a numerical solution of this multiobjective optimization problem and discusses the correspondence between the solution characteristics and flow regimes in gas–solid fluidization. This suggests that, while the most probable flow structures may correspond to the stable states predicted by the EMMS model, the noninferior solutions are in qualitative agreement with the observable flow structures under corresponding conditions. This demonstrates that both the dominant mechanisms and stability condition proposed for the EMMS model are physically reasonable and consistent, suggesting a general approach of describing complex systems with multiple dominant mechanisms.

Introduction

Gas–solid two-phase flow is widely encountered in nature and many engineering fields, such as chemical engineering, energy, and mining. The closure of its hydrodynamic model is difficult in theoretical and engineering research (Davidson, 1961; Grace & Clift, 1974; Hartge, Rensner, & Werther, 1988; Li, Tung, & Kwauk, 1988a; Toomey, 1952) owing to the complex multiscale structure (Li & Kwauk, 2001, 2003) of such flow. To address this challenge, Li et al. (Li, 1987; Li & Kwauk, 1994; Li et al., 1988a; Li, Tung, & Kwauk, 1988b) developed the energy-minimization multi-scale (EMMS) model for concurrent-up gas–solid two-phase flow as illustrated in Fig. 1.

The basic concepts and mathematical expressions of the EMMS model are summarized in Table 1, and further details on the derivations and physical meanings of the variables can be found in the literature (Li et al., 2005, 2013; Li & Kwauk, 1994).

For closure of the simplified hydrodynamic model, the methodology of the EMMS model introduces a stability condition by analyzing the extreme tendencies of the different dominant mechanisms involved; i.e., the gas tends to choose an upward path to minimize energy consumption,

$$W_{st}(X) = \left(\rho_p - \rho_f\right) g \left[(1-\varepsilon) U_g - f(1-f)(\varepsilon_f - \varepsilon_c) U_f\right] \rightarrow \min . \quad (1)$$

Meanwhile, particles tend to arrange themselves such that they minimize the potential energy and hence

$$\varepsilon(X) \rightarrow \min . \quad (2)$$

In a fluidized bed, however, neither the gas nor particles realize their own movement tendencies exclusively. There is thus a compromise in reaching a globally optimal state, which is

$$W_{st}(X) \rightarrow \min | \varepsilon(X) \rightarrow \min, \quad (15)$$

* Corresponding author at: State Key Laboratory of Multi-phase Complex Systems (MPCS), Institute of Processing Engineering (IPE), Chinese Academy of Sciences (CAS), Beijing 100190, China.
** Corresponding author.
E-mail addresses: wge@ipe.ac.cn (W. Ge), pzhang@pku.edu.cn (P. Zhang).

https://doi.org/10.1016/j.partic.2018.09.004

Nomenclature

D	Diameter of the fluidized bed, m
d_{cl}	Cluster diameter, m
d_p	Particle diameter, m
f	Dense phase fraction
G_s	Solids flow rate, kg/(m^2 s)
g	Gravitational acceleration, m/s^2
N_s	Mass specific energy consumption for the suspension of a particle, W/kg
N_{st}	Mass specific energy consumption for the suspension and transportation of a particle, W/kg
N_T	Mass specific total energy consumption for a particle, W/kg
N_t	Mass specific energy consumption for the transportation of a particle, W/kg
U_c	Superficial fluid velocity of the dense phase, m/s
U_f	Superficial fluid velocity of the dilute phase, m/s
U_g	Superficial fluid velocity, m/s
U_{mf}	Minimum fluidization velocity, m/s
U_p	Superficial particle velocity, m/s
U_{pc}	Superficial particle velocity of the dense phase, m/s
U_{pf}	Superficial particle velocity of the dilute phase, m/s
W_{st}	Volume specific energy consumption for the suspension and transportation of a particle, W/m^3
ε	Mean voidage
ε_c	Dense mean voidage
ε_f	Dilute mean voidage
ε_{max}	Maximum voidage for clustering
ε_{mf}	Voidage at minimum fluidization
μ	Fluid dynamic viscosity, kg/(m s)
ρ_f	Fluid density, kg/m^3
ρ_p	Particle real density, kg/m^3

and effectively, this can be simplified as a single extremum condition (Li, 1987; Li & Kwauk, 1994; Li et al., 1988a, 1988b):

$$N_{st}(X) = \frac{W_{st}(X)}{\rho_p(1-\varepsilon(X))} \rightarrow \min. \tag{16}$$

The solution to the EMMS model thus formulated has been obtained numerically and the predicted flow structures agree well with experimental results in terms of average characteristics (Du, Hu, Chen, Liu, & Ge, 2018; Li & Kwauk, 1994; Ge & Li, 2002). However, according to the EMMS principle (Li et al., 2013; Li, Huang, Chen, Ge, & Hou, 2018) later developed from the EMMS model, the multiobjective variational expression of the *compromise in competition* of the dominant mechanisms should be a more general and comprehensive description of the flow behaviors in the systems. As an indication, we note that, dynamically, flow structures different from the predictions of the EMMS model also exist in reality, but whether such existence is consistent with the EMMS model and principle is unknown. In fact, a precondition for answering this question is to solve the multiobjective optimization problem (MOP) of Eq. (15) exactly, which is the very purpose of this study.

Methods

This section introduces mathematical and numerical methods that are based on the classical theories of the MOP (Koopmans, 1951; Kuhn & Tucker, 1951; Lin & Dong, 1992).

Basic concepts of MOPs

MOPs, as the name suggests, are a type of optimization problem involving more than one objective function to be optimized simultaneously in a given constrained space. MOPs are found in many fields (Abakarov, Sushkov, Almonacid, & Simpson, 2009; Ganesan, Elamvazuthi, Shaari, & Vasant, 2013; Sendín, Alonso, & Banga, 2010; Shirazi, Aminyavari, Najafi, Rinaldi, & Razaghi, 2012), such as engineering, logistics, and economics, where optimal decisions need to be taken in the presence of trade-offs between two or more conflicting objectives.

In mathematical terms, an MOP can be formulated as

$$\begin{aligned} \min_{x\in\Omega}\ & f(x) = [f_1(x), f_2(x), \ldots, f_N(x)] \\ s.t.\ & h_j(x) = 0,\ j = 1,2,\ldots,k \\ & g_i(x) \le 0,\ i = 1,2,\ldots,m \\ & lb_d \le x_d \le ub_d,\ d = 1,2,\ldots,D \end{aligned}, \tag{17}$$

where $x = [x_1, x_2, \ldots, x_D]$ is a D-dimensional decision vector, $f(x)$ is the N-dimensional objective function, $h_j(x) = 0$ is the j-th constrained identity, $g_i(x) \le 0$ is the i-th constrained inequality, and $lb_d \le x_d \le ub_d$ indicates the reasonable range of the d-th decision vector component.

Accordingly, the solutions to an MOP can be defined rigorously. In fact, two types of solution can be defined in general. One type is the absolute optimal solutions that are a direct extension of the solution concept in single-objective optimization problems:

Denoting Ω as the constrained space and $x^* \in \Omega$, x^* is an absolute optimal solution if $f_i(x^*) \le f_i(x)$, $i = 1,2,\ldots,N$ for any other $x \in \Omega$.

The absolute optimal solution is an ideal solution in which the objective functions reach optimal values simultaneously. However, for an MOP, there is no absolute optimal solution in most cases owing to the competing or even contradictive objective functions, and only a set of relatively optimal solutions. The elements in this set are called Pareto-optimal solutions or non-inferior solutions, which are considered equally good and where none of the objective functions can be improved in value without reducing some of the other objective values. The mathematical definition of the Pareto-optimal solution or noninferior solution is (Koopmans, 1951):

Denoting Ω as the constrained space and $x^* \in \Omega$, x^* is a Pareto-optimal solution (also called a noninferior solution) if there exists no other $x \in \Omega$, s.t. $f_i(x) \le f_i(x^*)$, $i = 1,2,\ldots,N$.

It is worth mentioning that, apparently, if a point in the constrained space is not a noninferior solution, it is definitely not an absolute optimal solution of the MOP.

MOP in the EMMS model

From the previous subsection, it is apparent that, before introducing the stability condition of Eq. (16), the EMMS model subject to the competition of the dominant mechanisms of the gas and solid phases as expressed by the objective functions of Eq. (15), can be formulated as an MOP:

$$\begin{aligned} & W_{st} \rightarrow \min \mid \varepsilon \rightarrow \min \\ s.t.\ & F_j(x) = 0\ (j = 1,2,\ldots,6) \\ & U_{sc}(x) \ge 0,\ U_{sf}(x) \ge 0,\ U_{si}(x) \ge 0 \\ & lb_k \le x_k \le \mathrm{ub}_k\ (k = 1,2,\ldots,8) \end{aligned}, \tag{18}$$

where $x = X = \{\varepsilon_f, \varepsilon_c, f, U_f, U_c, U_{pf}, U_{pc}, d_{cl}\}$ is a vector comprising the eight independent variables of the EMMS model that

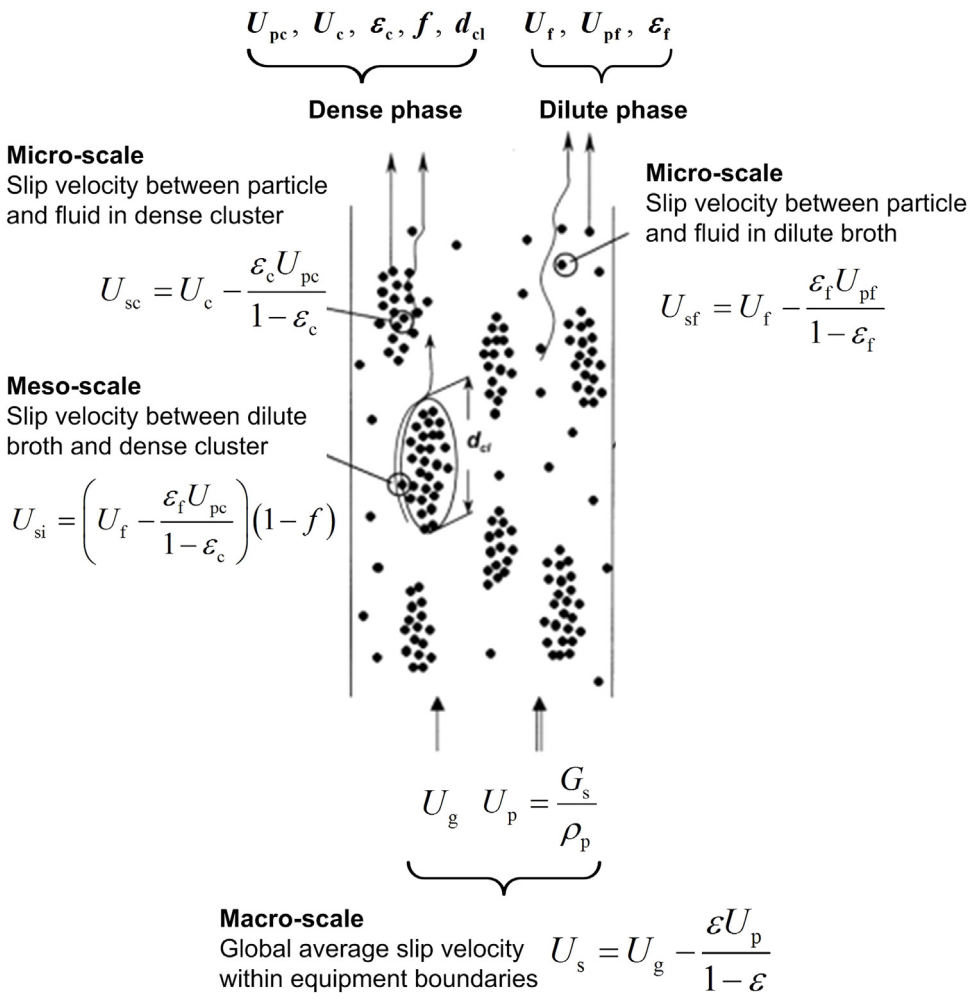

Fig. 1. Physical picture of the EMMS model and its variables (modified from Li and Kwauk (1994)).

are defined in Fig. 1, $F_j(x) = 0\,(j = 1,2,\ldots,6)$ are the six constraining equations in Table 1, $U_{sc}(x) \geq 0$, $U_{sf}(x) \geq 0$, and $U_{si}(x) \geq 0$ are three physical constraints ensuring nonnegative superficial slip velocities, and $lb_k \leq x_k \leq ub_k\,(k = 1,2,\ldots, 8)$ are the reasonable ranges of the eight components of the decision vector.

From the definitions, it is easily proved that if the MOP of Eq. (18) has an absolute optimal solution, the EMMS model has the same solution as the MOP. If the MOP has only noninferior solutions, the solution of the EMMS model always exists in the noninferior solution set. The MOP of Eq. (18) is, in fact, a more general expression of the compromise in competition of the two dominant mechanisms in a fluidization system, and the EMMS model with the stability condition of Eq. (16) may present its most probable results in reality. The conjunction, however, should be demonstrated by the solutions of both Eq. (18) and the EMMS model and compared with established understandings of the fluidization behaviors, which are discussed in the following sections.

Numerical method for solving the MOP in the EMMS model

A specific numerical scheme (Ge & Li, 2002) is employed to solve the above MOP in this work. The main idea of the algorithm is to build a two-dimensional constrained space Ω, store the corresponding variable value and search for the solution according to the definition of the noninferior solution. The steps of the algorithm are as follows.

1. Select the operation parameter (G_s,U_g).
2. Traverse ε_c^0 and ε_f^0 in $[\varepsilon_{mf}, \varepsilon_{max}]$.
3. Calculate U_{sf} from Eq. (5).
4. Select a trial value of $f \in [0, 1]$.
5. Calculate U_{sc} from Eqs. (6) and (7).
6. Use U_{sf} and U_{sc} to determine U_f, U_c, U_{pf}, U_{pc}, and U_{si} from Eqs. (3)–(8).
7. Calculate U_{si} according to its definition, Eq. (11).
8. Denote by ΔU_{si} the difference in U_{si} between Steps 6 and 7. If ΔU_{si} is not sufficiently small, return to step 4 and select a new f; otherwise, regard $\left(\varepsilon_c^0, \varepsilon_f^0\right)$ as a solution in the two-dimensional constrained space Ω, store the values of $W_{st}\left(\varepsilon_c^0, \varepsilon_f^0\right)$ and $\varepsilon_{st}\left(\varepsilon_c^0, \varepsilon_f^0\right)$ and return to Step 2 to continue traversing ε_c and ε_f.
9. Search $\left(\varepsilon_c^*, \varepsilon_f^*\right) \in \Omega$. If there is no other $(\varepsilon_c, \varepsilon_f) \in \Omega$, *s.t.* $W_{st}(\varepsilon_c, \varepsilon_f) < W_{st}\left(\varepsilon_c^*, \varepsilon_f^*\right)$ and $\varepsilon_{st}(\varepsilon_c, \varepsilon_f) < \varepsilon_{st}\left(\varepsilon_c^*, \varepsilon_f^*\right)$, then $\left(\varepsilon_c^*, \varepsilon_f^*\right)$ is a solution of the MOP.

Results and discussion

In this section, using the physical properties, geometry and operating conditions listed in Table 1 and the algorithm described above, we first study the distributing characteristics of solutions for the MOP under different operating conditions and describe the physical meaning associated with the flow regimes and then analyze

Table 1
Formulation of the EMMS model (Li et al., 2005, 2013; Li & Kwauk, 1994) and specifications of the calculation conditions.

Mass balance for the gas phase:

$$U_g = fU_c + (1-f)U_f, \tag{3}$$

the gas flow through the whole cross-section of the vessel equals the sum of the gas flow through the dilute and dense phases

Mass balance for the solid phase:

$$U_p = (1-f)U_{pf} + fU_{pc}, \tag{4}$$

the solid flow through the whole cross-section of the vessel equals the sum of the mass flow through the dilute and dense phases

Force balance for the dilute phase:

$$\frac{3}{4}C_{df}\frac{1-\varepsilon_f}{d_p}\rho_f U_{sf}^2 = (1-\varepsilon_f)(\rho_p-\rho_f)g, \tag{5}$$

the effective weight of the particles in the dilute phase equals the drag from the gas in the dilute phase

Force balance for the dense phase:

$$\frac{3}{4}C_{dc}\frac{1-\varepsilon_c}{d_p}\rho_f U_{sc}^2 f + \frac{3}{4}C_{di}\frac{f}{d_{cl}}\rho_f U_{si}^2 = f(1-\varepsilon_c)(\rho_p-\rho_f)g, \tag{6}$$

the effective weight of the dense phase particles equals the sum of the drag from the gas in the dense and dilute phases

Pressure balance:

$$C_{df}\frac{1-\varepsilon_f}{d_p}\rho_f U_{sf}^2 + \frac{f}{1-f}C_{di}\frac{1}{d_{cl}}\rho_f U_{si}^2 = C_{dc}\frac{1-\varepsilon_c}{d_p}\rho_f U_{sc}^2, \tag{7}$$

the dense phase pressure drop is balanced by that of the dilute phase plus the interphase

Cluster diameter correlation:

$$d_{cl} = \frac{g d_p\left[\frac{U_p}{1-\varepsilon_{max}} - \left(U_{mf} + \frac{\varepsilon_{mf}}{1-\varepsilon_{mf}}U_p\right)\right]}{N_{st}\frac{\rho_p}{\rho_p-\rho_f} - g\left(U_{mf} + \frac{\varepsilon_{mf}}{1-\varepsilon_{mf}}U_p\right)}, \tag{8}$$

the diameter of a cluster is inversely proportional to the rate of energy input

The stability condition (Ge & Li, 2002):

$$N_{st} = \frac{(\rho_p-\rho_f)g}{\rho_p(1-\varepsilon)}\left[f(1-\varepsilon)U_c + (1-f)(1-\varepsilon_f)U_f + f(1-f)^2(\varepsilon_f-\varepsilon_c)U_f\right] \to \min \tag{9}$$

Mean voidage:

$$\varepsilon = f\varepsilon_c + (1-f)\varepsilon_f \tag{10}$$

Superficial slip velocity:

$$U_{sc} = U_c - \frac{\varepsilon_c U_{pc}}{1-\varepsilon_c},\ U_{sf} = U_f - \frac{\varepsilon_f U_{pf}}{1-\varepsilon_f},\ U_{si} = \left(U_f - \frac{\varepsilon_f U_{pc}}{1-\varepsilon_c}\right)(1-f). \tag{11}$$

Reynolds numbers:

$$Re_c = \frac{\rho_f d_p U_{sc}}{\mu},\ Re_f = \frac{\rho_f d_p U_{sf}}{\mu},\ Re_f = \frac{\rho_f d_p U_{sf}}{\mu},\ Re_i = \frac{\rho_f d_{cl} U_{si}}{\mu} \tag{12}$$

Drag coefficient for a single particle or cluster (Schiller, 1933):

$$C_{dc0} = \frac{24}{Re_c} + \frac{3.6}{Re_c^{0.313}},\ C_{df0} = \frac{24}{Re_f} + \frac{3.6}{Re_f^{0.313}},\ C_{di0} = \frac{24}{Re_i} + \frac{3.6}{Re_i^{0.313}} \tag{13}$$

Drag coefficient for fluidized particles or clusters (Wen & Yu, 1966):

$$C_{dc} = C_{dc0}\varepsilon_c^{-4.7},\ C_{df} = C_{df0}\varepsilon_f^{-4.7},\ C_{di} = C_{di0}(1-f)^{-4.7} \tag{14}$$

Gravitational acceleration: $g = 9.8\ m/s^2$, maximum voidage for clustering: $\varepsilon_{max} = 0.9997$. Physical properties of FCC catalyst particle and air in the calculations of this work: $d_p = 54\ \mu m$, $\rho_p = 929.5\ kg/m^3$, $\varepsilon_{mf} = 0.5$, $\rho_f = 1.1795\ kg/m^3$, $\mu = 1.8872 \times 10^{-5}\ kg/(m\,s)$, $U_{mf} = 0.002\ m/s$. *Note*: U_{mf} is obtained from calculation according to the formula: $\frac{3}{4}C_{df}\frac{1-\varepsilon_{mf}}{d_p}\rho_f U_{mf}^2 = (1-\varepsilon_f)(\rho_p-\rho_f)g$.

the relationship between the solutions of the MOP and the EMMS model.

Characteristics of the solutions of the MOP under different operating conditions

For the operating conditions $G_s \in [100, 700]$, $U_g \in [0.01, 8]$, the numerical results show that if the MOP has a solution, it always exists on the boundaries of Ω. According to the locations of the solutions in Ω, the operating conditions can be classified into several regimes as shown in Fig. 2. In Region 1, the constrained space is an empty set and the MOP has no solution. In Regions 2–5, as W_{st} and ε reach minimum values at different locations, the MOP only has noninferior solutions. In Region 2, the noninferior solutions exist only on the bottom boundary $\varepsilon_c = \varepsilon_{mf}$, $\varepsilon_f \in [\varepsilon_{mf}, \varepsilon_{max}]$ as shown in Fig. 3(a). Region 3 is a transitional region between Regions 2 and 4, and the noninferior solutions exist on both the bottom boundary $\varepsilon_c = \varepsilon_{mf}$, $\varepsilon_f \in [\varepsilon_{mf}, \varepsilon_{max}]$ and the right boundary $\varepsilon_c \in [\varepsilon_{mf}, \varepsilon_{max}]$, $\varepsilon_f = \varepsilon_{max}$ as shown in Fig. 3(b). In Regions 4 and 5, the positions of noninferior solutions are on the right boundary in Ω as shown in Fig. 3(c) and (d).

Physical meaning of the solutions of the MOP associated with the flow regime

Physically, in Region 1, as the gas phase passes upward through a bed of particles at relatively low velocity, the drag of the gas phase is not large enough to support the whole weight of the solid particles. This corresponds to, for example, fixed beds, and there are no two-phase solutions. In Regions 2, 3, 4 and 5, neither the gas nor the particles realize their own movement tendencies exclusively; there must be a compromise and, correspondingly, the MOP has noninferior solutions. In Region 2, the dilute phase voidage varies ($\varepsilon_f \in [\varepsilon_{mf}, \varepsilon_{max}]$) but the dense phase is always at minimum fluidization ($\varepsilon_c = \varepsilon_{mf}$), which agrees well with the flow pattern of (generalized) bubbling fluidization under the operation conditions of this region. The dilute phase particles are mostly in bubble wakes. Then, in Region 3 with higher U_g, the dense phase becomes sparser ($\varepsilon_c \geq \varepsilon_{mf}$), which conforms well to the transition from bubbling to turbulent fluidization, where bubbles exhibit a variety of irregular shapes and complex dynamics. In Region 4, as the gas velocity continues to increase, the voidage of dilute phase reaches a maximum ($\varepsilon_f = \varepsilon_{max}$), which corresponds to fast fluidization where the bubbles completely break up and isolated particle clusters dominate the flow. In Region 5, with ε_f remaining at ε_{max}, ε_c also jumps from ε_{mf} to a larger value ($\varepsilon_c > \varepsilon_{mf}$), which is characteristic of dilute transport, and the jump in ε_c corresponds to the choking phenomenon.

Solutions of the MOP corresponding to flow regime transitions

Considering any given $G_s \in [100, 700]$, with an increase in $U_g \in [0.01, 8]$, along the right boundary of Ω, the locations of the minimums of W_{st} jump from the lower corner $\varepsilon_c = \varepsilon_{mf}$, $\varepsilon_f = \varepsilon_{max}$ to an

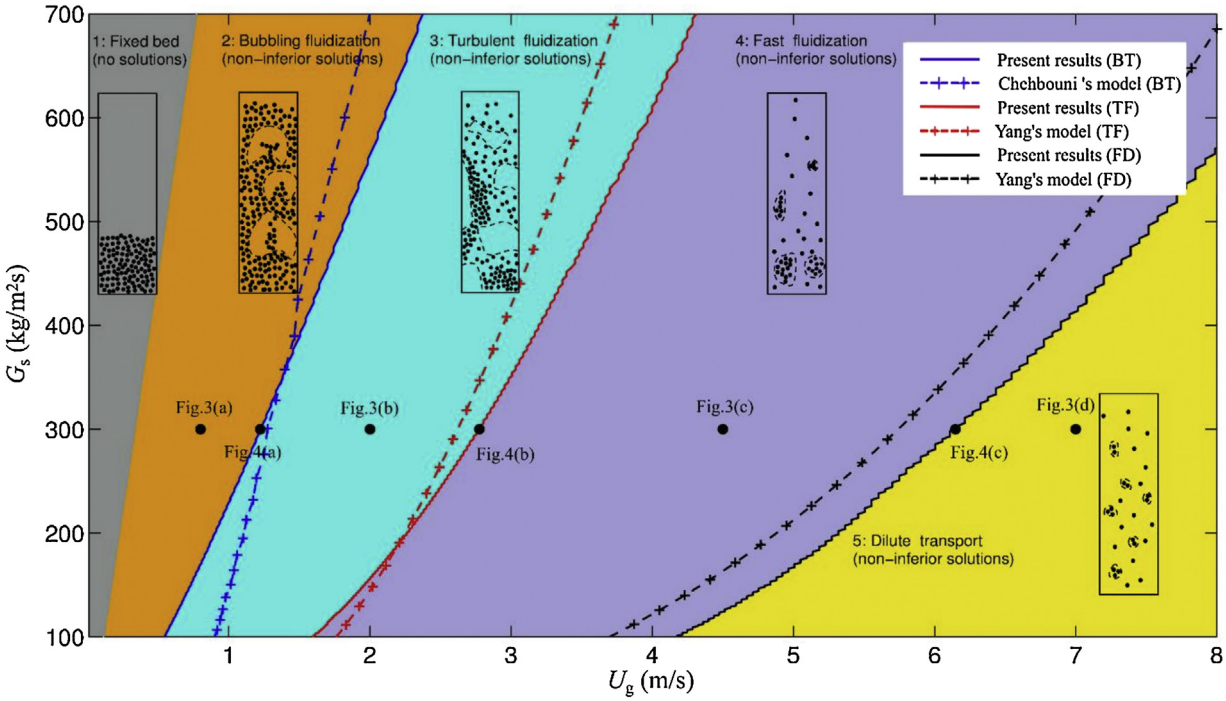

Fig. 2. Relationship between the solutions of the MOP and the flow regimes under different operating conditions.

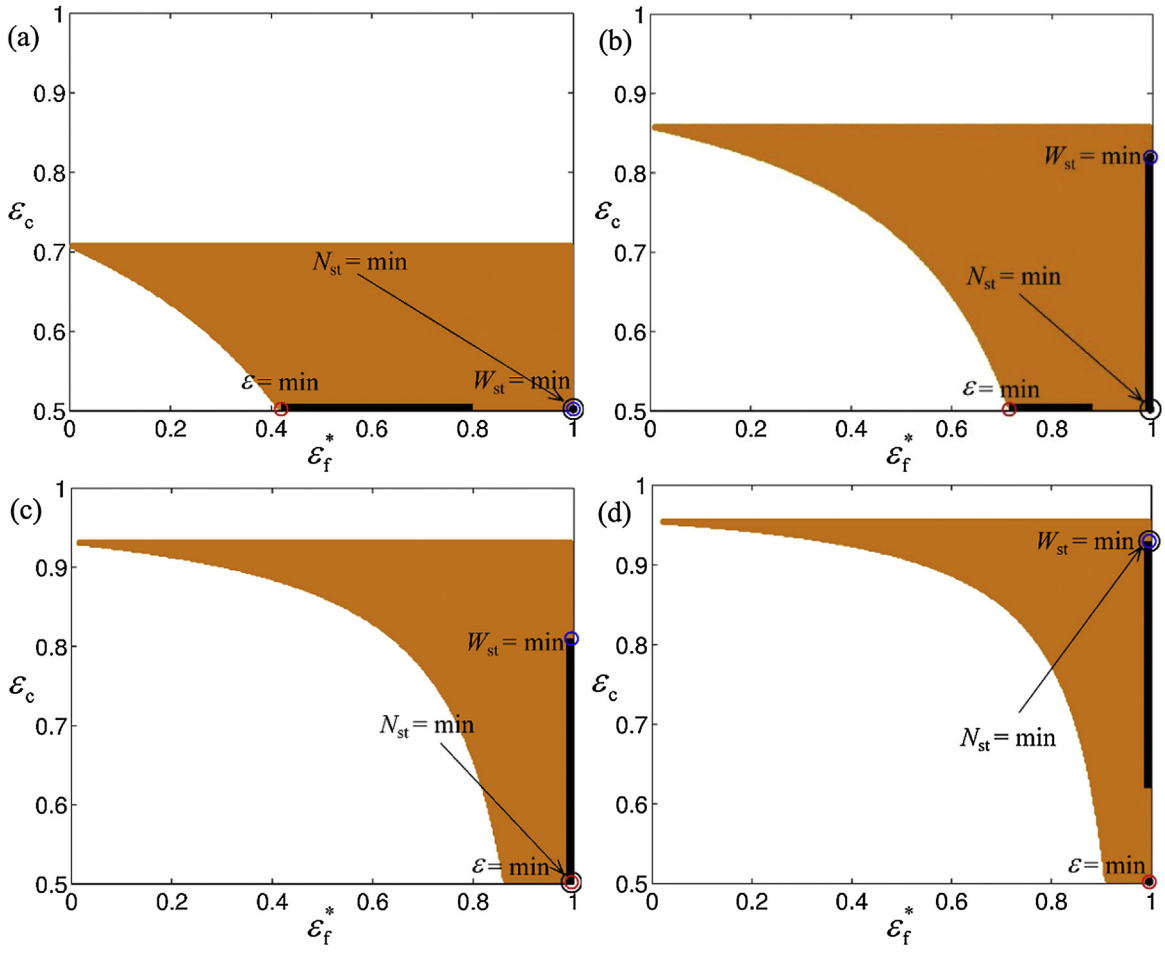

Fig. 3. Types of solution for the MOP under different operating conditions: (a) $G_s = 300\ \mathrm{kg/(m^2\ s)}$, $U_g = 0.8\ \mathrm{m/s}$; (b) $G_s = 300\ \mathrm{kg/(m^2\ s)}$, $U_g = 2.0\ \mathrm{m/s}$ (c) $G_s = 300\ \mathrm{kg/(m^2\ s)}$, $U_g = 4.5\ \mathrm{m/s}$; and (d) $G_s = 300\ \mathrm{kg/(m^2\ s)}$, $U_g = 7.0\ \mathrm{m/s}$. The abscissa axis is the relative dilute phase voidage defined as $\varepsilon_f^* = (\varepsilon_f - \varepsilon_c)/(\varepsilon_{max} - \varepsilon_c)$ while the ordinate axis is ε_c. The orange region represents the constrained space. ε, W_{st}, and N_{st} respectively reach their minimums at the red, blue and black circles. The black bold line represents the noninferior solutions of the MOP.

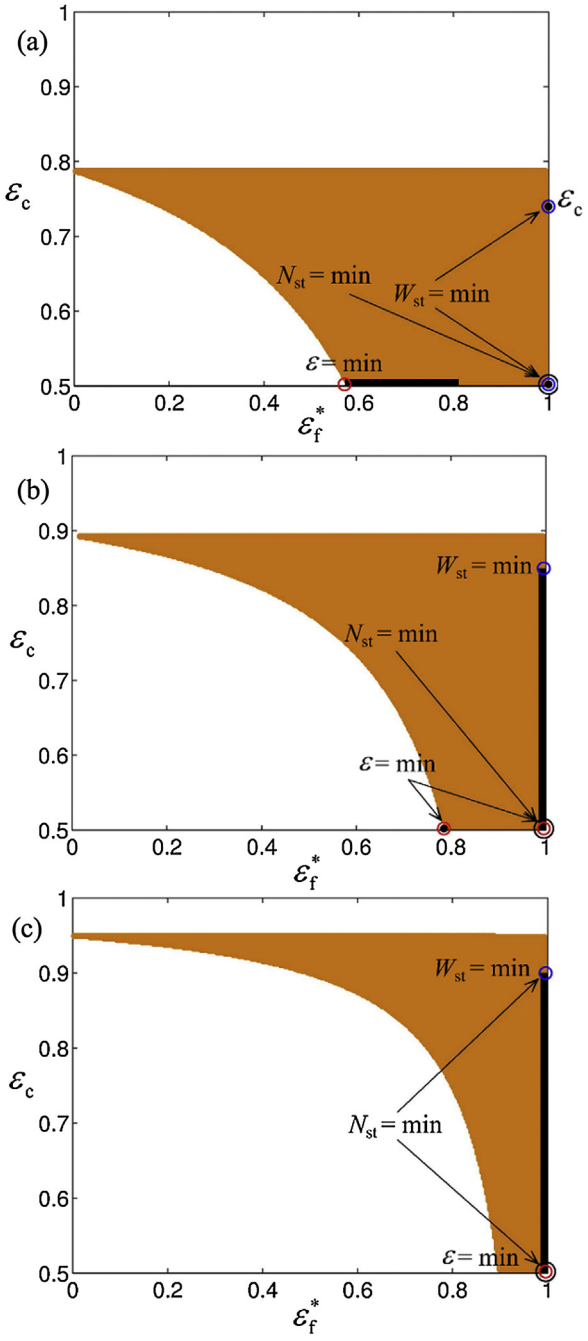

Fig. 4. Solutions of the MOP corresponding to flow regime transition: (a) $G_s = 300\ kg/(m^2\ s)$, $U_g = 1.2\ m/s$; (b) $G_s = 300\ kg/(m^2\ s)$, $U_g = 2.8\ m/s$; and (c) $G_s = 300\ kg/(m^2\ s)$, $U_g = 6.1\ m/s$.

upper point $\varepsilon_c \gg \varepsilon_{mf}$, $\varepsilon_f = \varepsilon_{max}$. The blue solid line in Fig. 2 represents the operating conditions corresponding to these jumps. On this line, W_{st} has two minimums in Ω as seen in Fig. 4(a). As the gas velocity continues to increase, the location of the minimum of ε along the bottom boundary of Ω jumps to the right boundary. The red solid line in Fig. 2 represents the operating conditions corresponding to these jumps. On this line, ε has two minimums as seen in Fig. 4(b); one is at $\varepsilon_c = \varepsilon_{mf}$, $\varepsilon_f \ll \varepsilon_{max}$ and the other is at $\varepsilon_c = \varepsilon_{mf}$, $\varepsilon_f = \varepsilon_{max}$. In addition, the black solid line in Fig. 2 represents the operating conditions corresponding to the jump of N_{st}. On this line, N_{st} has two minimums in Ω as seen in Fig. 4(c). These jumps have physical counterparts in fluidization engineering, as discussed below.

Several correlations for the flow regime transition have been mentioned in the literature; e.g., Yang's model (Yang, 1983) for the transition between the turbulent fluidization region and fast fluidization region (TF) is

$$\begin{aligned} U_t &= \left[\frac{4gd_p\left(\rho_p-\rho_f\right)}{3\rho_f C_{d0}}\right]^{0.5}, \\ \frac{2gD(\varepsilon_{mid}^{-4.7}-1)}{(U_{TF}-U_t)^2} &= 68100\left(\frac{\rho_f}{\rho_p}\right)^{2.20}, \\ G_{TF} &= (U_{TF}-U_t)\,\rho_p(1-\varepsilon_{mid}), \end{aligned} \tag{19}$$

where D is the diameter of the fluidized bed and is set to 0.09.

Yang's model (Yang, 2004) for the transition between the fast fluidization region and dilute transport region (FD) is

$$G_{FD} = 3.8364U_{FD}^{2.4938}. \tag{20}$$

Additionally, employing the concept of generalized fluidization and Chehbouni's model (Chehbouni, Chaouki, Guy, & Klvana, 1995), a correlation for the transition between the bubbling fluidization region and turbulent fluidization region (BT) can be proposed:

$$\begin{aligned} U_{BT} &= (U_0)_{G_s=0} + \frac{\varepsilon}{1-\varepsilon}\frac{G_s}{\rho_p}, \\ \frac{(U_0)_{G_s=0}}{\sqrt{gD}} &= 0.463Ar^{0.145}, \\ Ar &= \frac{gd_p\rho_f\left(\rho_p-\rho_f\right)}{\mu^2}. \end{aligned} \tag{21}$$

As shown in Fig. 2, the regime transitions predicted using the solutions of the MOP based on the EMMS model agree qualitatively well with the correlations above.

Relationship between the solutions of the MOP and the EMMS model

The numerical results suggest that the relationship of the solutions of the EMMS model and the corresponding MOP depends on the operating conditions. In Regions 2–5 of Fig. 2, the MOP has noninferior solutions and the solutions of the EMMS model exist in the noninferior solution set. It is worth noting that the minimums of W_{st} and ε are always located at the two endpoints of the noninferior solution set while the location of the minimum of N_{st} is affected by the compromise between $W_{st}(x) \to \min$ and $\varepsilon(x) \to \min$. In Region 2, N_{st} and W_{st} reach their minimums at the same location, as seen in Fig. 3(a). In Region 3, the locations of the minimums of W_{st}, ε, and N_{st} are different, as seen in Fig. 3(b). In Region 4, N_{st} and ε reach their minimums at the same location, as seen in Fig. 3(c). In Region 5, the locations of the minimums of N_{st} are closer to the location of the minimum of W_{st} as seen in Fig. 3(d). The results show clearly that $W_{st}(x) \to \min$ and $\varepsilon(x) \to \min$ are reasonable reflections of the extremum tendencies of the two phases, as indicated by the distribution of the noninferior solutions of the MOP about them, and $N_{st}(x) \to \min$ is indeed a good reflection of the compromise between them, with a logical distribution of the flow regimes in the constrained space. These findings are a further demonstration of the validity of the EMMS models.

In reality, we can observe many states of the system other than the predictions of the EMMS model, and from this work we understand that they are actually the noninferior solutions of the MOP expressing the multiple dominant mechanisms. As the stability condition in the EMMS model expresses the result of compromising the dominant mechanisms, it is reasonable to conjecture that the solutions from the EMMS model represent the most probable

states among them. Of course, rigorous verification of this conjecture remains the subject of future experimental and simulation works.

Conclusions

In this paper, first, on the basis of the stability condition in the EMMS model, we explored the MOP with $W_{st}(X) \rightarrow \min | \varepsilon(X) \rightarrow \min$ under different operating conditions. The theoretical and numerical results show that, in most cases, W_{st} and ε have different monotonicities in Ω and the MOPs only have the noninferior solutions, which suggests that the system can reach multiple stable states under the same operational parameters. All noninferior solutions studied so far are on the boundaries of Ω. All minimums of W_{st} and ε are located at the two endpoints of the noninferior solution set, while the location of the minimum of N_{st} is affected by the compromise between $W_{st}(x) \rightarrow \min$ and $\varepsilon(x) \rightarrow \min$. Additionally, we found a good physical explanation for different solution regimes of the MOP, which is helpful in explaining the flow regime transitions from the angle of the EMMS model.

The results of this study further explain the mathematical and physical meanings of the stability condition in the EMMS model, verify the reasonableness of the model and help to improve the model. Furthermore, this paper suggests a new approach of characterizing complex systems controlled by multiple mechanisms.

Acknowledgement

This work is financially supported by the National Natural Science Foundation of China under grant No. 91434201; the Key Research Program of Frontier Science, CAS, under grant No. QYZDJ-SSW-JSC029, and the Transformational Technologies for Clean Energy and Demonstration, Strategic Priority Research Program of the Chinese Academy of Sciences under grant No. XDA 21030700. We thank Prof. Jinghai Li of IPE for illuminative discussions and insightful suggestions.

References

Abakarov, A., Sushkov, Y., Almonacid, S., & Simpson, R. (2009). Multiobjective optimization approach: Thermal food processing. *Journal of Food Science*, *74*(9), E471–E481.

Chehbouni, A., Chaouki, J., Guy, C., & Klvana, E. D. (1995). Effets de differents parametres sur les vitesses de transition de la fluidisation en regime turbulent. *The Canadian Journal of Chemical Engineering*, *73*(1), 41–50.

Davidson, J. F. (1961). Symposium on fluidization-discussion. *Transactions of the Institution of Chemical Engineers*, *39*, 223–240.

Du, M. J., Hu, S. W., Chen, J. H., Liu, X. H., & Ge, W. (2018). Extremum characteristics of energy consumption in fluidization analyzed by using EMMS. *Chemical Engineering Journal*, *342*, 386–394.

Ganesan, T., Elamvazuthi, I., Shaari, K. Z. K., & Vasant, P. (2013). Swarm intelligence and gravitational search algorithm for multi-objective optimization of synthesis gas production. *Applied Energy*, *103*, 368–374.

Ge, W., & Li, J. H. (2002). Physical mapping of fluidization regimes—The EMMS approach. *Chemical Engineering Science*, *57*(18), 3993–4004.

Grace, J. R., & Clift, R. (1974). On the two-phase theory of fluidization. *Chemical Engineering Science*, *29*(2), 327–334.

Hartge, E. U., Rensner, D., & Werther, J. (1988). Solids concentration and velocity patterns in circulating fluidized beds. *Circulating Fluidized Bed Technology: Proceedings of the Second International Conference*, 165–180.

Koopmans, T. (1951). *Activity analysis of production and allocation*. New York: John Wiley and Sons.

Kuhn, H. W., & Tucker, A. W. (1951). Nonlinear programming. *Proceedings of the 2nd Berkeley Symposium on Mathematical Statistics and Probability*, 481–492.

Li, J. H. (1987). *Multi-scale modeling and method of energy minimization for particle–fluid two-phase flow (doctoral dissertation)*. China: Institute of Chemical Metallurgy, Academia Sinica (in Chinese).

Li, J. H., Ge, W., Wang, W., Yang, N., Liu, X., Wang, L., et al. (2013). *From multiscale modeling to meso-science*. Heidelberg: Springer.

Li, J. H., Huang, W. L., Chen, J. H., Ge, W., & Hou, C. F. (2018). Mesoscience based on the EMMS principle of compromise in competition. *Chemical Engineering Journal*, *333*, 327–335.

Li, J. H., & Kwauk, M. (1994). *Particle–fluid two-phase flow: The energy-minimization multi-scale method*. Beijing: Metallurgical Industry Press.

Li, J. H., & Kwauk, M. (2001). Multiscale nature of complex fluid–particle systems. *Industrial & Engineering Chemistry Research*, *40*(20), 4227–4237.

Li, J. H., & Kwauk, M. (2003). Exploring complex systems in chemical engineering—The multi-scale methodology. *Chemical Engineering Science*, *58*(3–6), 521–535.

Li, J. H., Ouyang, J., Gao, S. Q., Ge, W., Yang, N., & Song, W. L. (2005). *Multi-scale modeling of complex particle-fluid system*. Beijing: Science Press.

Li, J. H., Tung, Y. K., & Kwauk, M. (1988a). Energy transport and regime transition in particle–fluid two-phase flow. *Circulating Fluidized Bed Technology: Proceedings of the Second International Conference*, 75–87.

Li, J. H., Tung, Y. K., & Kwauk, M. (1988b). Method of energy minimization in multi-scale modeling of particle–fluid two-phase flow. *Circulating Fluidized Bed Technology: Proceedings of the Second International Conference*, 89–103.

Lin, C. Y., & Dong, J. L. (1992). *Method and theory of multi-objective optimization*. Jilin: Jilin Education Press (in Chinese).

Schiller, L. (1933). Über die grundlegenden Berechnungen bei der Schwerkraftaufbereitung. *Zeitschrift des Vereines Deutscher Ingenieure*, *77*, 318–321.

Sendín, J. O. H., Alonso, A. A., & Banga, J. R. (2010). Efficient and robust multi-objective optimization of food processing: A novel approach with application to thermal sterilization. *Journal of Food Engineering*, *98*(3), 317–324.

Shirazi, A., Aminyavari, M., Najafi, B., Rinaldi, F., & Razaghi, M. (2012). Thermal–economic–environmental analysis and multi-objective optimization of an internal-reforming solid oxide fuel cell–gas turbine hybrid system. *International Journal of Hydrogen Energy*, *37*(24), 19111–19124.

Toomey, R. D. (1952). Gaseous fluidization of solid particles. *Chemical Engineering Progress*, *48*, 220–226.

Wen, C. Y., & Yu, Y. H. (1966). Mechanics of fluidization. *Chemical Engineering Progress Symposium Series*, *62*, 100–111.

Yang, W. C. (1983). Criteria for choking in vertical pneumatic conveying lines. *Powder Technology*, *35*(2), 143–150.

Yang, W. C. (2004). "Choking" revisited. *Industrial & Engineering Chemistry Research*, *43*(18), 5496–5506.